ACS Catalysis

pubs.acs.org/acscatalysis
Research Article

Tailoring Cu-Based Nanoalloys for Highly Selective Electrochemical Urea Synthesis from CO_2 and Nitrate

Hao Zhang, Jinjie Liu, Zhihang Xu, Yuanzhi Bu, Tai-Sing Wu, Wei-Min Tu, Yun-Liang Soo, Cong Lin, Ye Zhu, Qiong Lei,* Jun Yin,* and Tsz Woon Benedict Lo*

Cite This: ACS Catal. 2025, 15, 8966−8978

ABSTRACT: The current carbon and nitrogen cycles, as driven by human activity, are characterized by high energy consumption, especially in the context of excessive CO_2 emissions. To establish a commercially viable electrochemical coupling of nitrate and CO_2 for urea production, developing a highly selective catalyst is crucial. In this study, we synthesized a series of ultrafine Cu-M (M = Bi, In, and Pb) nanoalloy catalysts using electrodeposition. We employed a phenanthroline-mediated approach to carefully control the dopant composition and nanoalloy size by regulating the electrodeposition kinetics. Our ultrafine Cu−$Bi_{0.1}$ catalyst achieved a significantly enhanced Faradaic efficiency for urea production of 89.4% at −1.0 V vs RHE, compared to 41.5% for the Cu control. Operando Raman and Fourier-transform infrared spectroscopy provided compelling evidence supporting our catalytic findings. The remarkable selectivity to urea observed with our Cu−$Bi_{0.1}$ catalyst originates from the stabilization of *CO and *NO_2 intermediates. Through extensive theoretical calculations, we found that the presence of Bi in the Cu domain enhances urea formation both thermodynamically and kinetically. This work presents a promising chemical protocol for designing next-generation nanoalloy catalytic materials with enhanced properties.

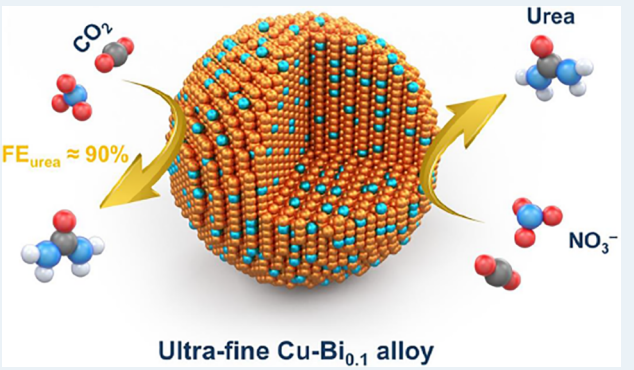

KEYWORDS: *urea, nitrate reduction, carbon dioxide reduction, Cu−Bi alloy, electrocatalysis, C−N coupling*

INTRODUCTION

Urea ($CO(NH_2)_2$), a crucial nitrogen-based fertilizer, plays a vital role in bolstering global crop yields and ensuring food security for humanity.[1,2] However, the conventional industrial manufacturing process for urea, known as the Bosch-Meiser process, involves combining CO_2 and liquid ammonia under harsh conditions of high temperature (150−200 °C) and pressure (150−250 bar).[3] Additionally, the energy-intensive Haber-Bosch process, which underpins ammonia synthesis for urea production, heavily relies on fossil fuels and contributes to approximately 2% of worldwide natural gas usage and 1% of global CO_2 emissions.[4] In light of the mounting pressures for sustainable development, the current carbon and energy footprint associated with urea synthesis falls short of social demands. Thus, the development of sustainable technologies for producing 'green urea' under mild conditions becomes imperative.

Electrochemical routes offer a promising alternative for the conversion of feedstocks into valuable chemicals, utilizing renewable energy sources.[5,6] Inspired by the electrochemical reduction of N_2 to ammonia, researchers have pursued a new avenue for urea electrosynthesis through the coreduction of N_2 and CO_2 in ambient aqueous solutions.[7] However, the direct activation of N_2 coupled with CO_2 faces limitations, including low selectivity (not exceeding 20%) due to the high overpotential required to dissociate the robust C═O (806 kJ mol^{-1}) and N≡N (941 kJ mol^{-1}) bonds, as well as strong competition from parallel reactions.[8,9] In recent studies, the scientific community has explored the coreduction of CO_2 with nitrate (NO_3^-) or nitrite (NO_2^-) as a viable approach for urea electrosynthesis (as shown in Figure 1). This approach offers a potential solution to the global challenge of nitrate pollution from sources like agricultural runoff and industrial wastewater, where traditional treatment technologies are often costly and can generate secondary pollutants.[10−12] Our research innovatively converts NO_3^- into high-value urea, which not only provides a new avenue for pollutant resource utilization but also offers the dual benefits of carbon emission reduction. However, achieving a breakthrough with a high Faradaic

Received: March 19, 2025
Revised: April 25, 2025
Accepted: April 28, 2025
Published: May 13, 2025

Figure 1. Scheme illustrating the synthesis of "gray urea" through conventional industrial approaches compared to the production of "green urea" via electrochemical coreduction of CO_2 and nitrate.

efficiency of urea (FE_{urea}) surpassing 75% remains a significant challenge that greatly limits resource utilization.

The electrochemical reduction process involved in urea synthesis is remarkably complex, involving a 16-electron transfer and over 70 intermediate steps.[6,13] Despite extensive research, the scientific community has yet to reach a consensus on the precise mechanism of urea electrosynthesis. A key area of debate centers around the coupling of various C- and N-containing intermediates. The favored mechanism for urea synthesis is heavily influenced by the specific electrocatalysts employed and their morphologies.[12,14] Cu-based materials have emerged as particularly promising due to their superior selectivity in producing C_{2+} products during CO_2 reduction.[15−17] Consequently, Cu-based catalysts have been frequently explored for the electrochemical coupling of CO_2 and nitrate. Different studies proposed distinct coupling mechanisms based on the catalytic systems used. For example, Li and co-workers suggested the coupling between *CO and $*NO_2$ species over a Cu−W bimetallic surface, while Sargent and co-workers proposed the coupling between $*CO_2$ and $*NO_2$ on a Cu−Zn hybrid catalyst with a Zn surface.[18] Alloying or doping Cu with other metallic elements, such as Sn, Zn, Bi, In, and Pb, has proven to be an effective strategy for tuning the adsorption and stabilization of crucial reaction intermediates. The addition of Sn to the Cu lattice has been found to preferentially stabilize *CHO intermediates, enhancing the selectivity toward C_{2+} products over methane in CO_2 reduction.[19,20] Moreover, the incorporation of Zn, Bi, In, and Pb into Cu has demonstrated the ability to strengthen the binding of *COOH species, which are crucial intermediates in the electrochemical reduction of CO_2 to valuable hydrocarbons and alcohols.[21−24] However, a systematic investigation of dopant composition and nanoparticle morphology with subtle control of Cu-based domains has not fully been explored.

Despite the promising advances, several challenges remain in the electrochemical synthesis of urea from CO_2 and nitrate. One of the primary hurdles is the need for highly active and selective electrocatalysts that can efficiently facilitate the complex multielectron transfer process. Additionally, the stability and durability of these catalysts under operating conditions are crucial for practical applications. Understanding the fundamental mechanisms underlying the electrochemical reduction process is essential for designing more effective catalysts and optimizing reaction conditions. Furthermore, the economic viability and scalability of the electrochemical route for urea synthesis need to be carefully assessed. This includes evaluating the cost of electrocatalysts, the efficiency of the electrochemical cells, and the overall energy consumption. Integrating renewable energy sources, such as solar or wind power, to drive the electrochemical reactions can further enhance the sustainability of the process.

In this study, we present a robust protocol for developing Cu-M ultrafine nanoalloys using a modified electrodeposition approach, which has shown promising catalytic performance in 'green urea' electrosynthesis. Unlike previous research that employed heterostructured or bulk Cu-M phases, our method produces homogeneous Cu-M nanoalloys (M = Bi, In, and Pb) with precisely controlled dopant composition, distribution, and morphology. This synthetic strategy leverages principles of electrochemistry and coordination chemistry to achieve precise control over electrodeposition kinetics. This results in uniformly sized nanoparticles (around 10 nm) with a homogeneous distribution of M within the Cu domain. Our $Cu−Bi_{0.1}$ nanoalloy exhibited outstanding performance, achieving a Faradaic efficiency for urea (FE_{urea}) of 89.4% at −1.0 V vs RHE, surpassing the efficiency of our control Cu sample by more than double. Integrated *operando* Raman and infrared spectroscopy studies revealed that the preferential stabilization of key intermediates *CO and $*NO_2$ on $Cu−Bi_{0.1}$

https://doi.org/10.1021/acscatal.5c01960
ACS Catal. 2025, 15, 8966−8978

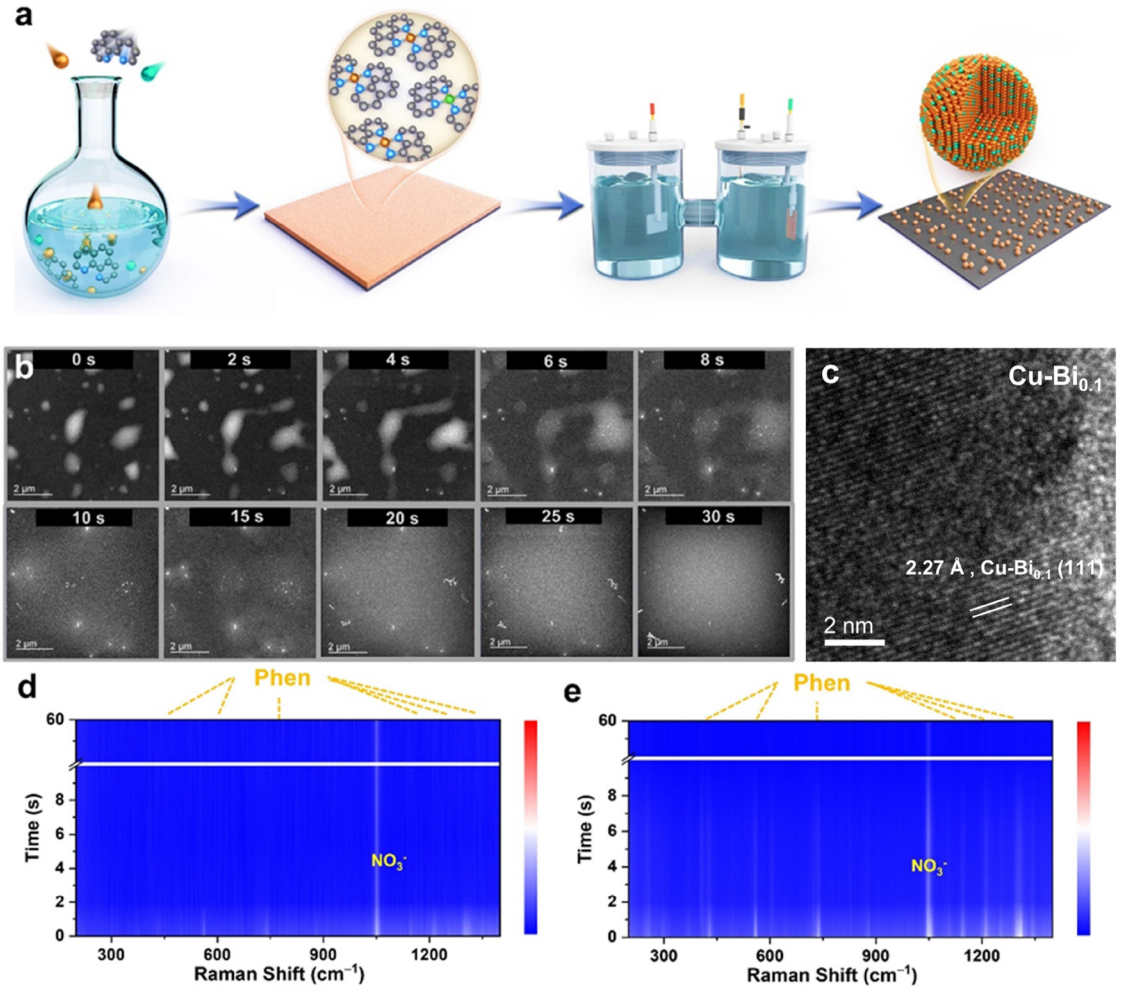

Figure 2. (a) Schematic representation of the modified electrodeposition synthesis of ultrafine Cu-$M_{0.1}$ nanoalloys used in this study. (b) In-situ TEM images 'recording' the electrodeposition process of Cu−$Bi_{0.1}$. (c) HRTEM image. In-situ Raman spectroscopy studying the electrodeposition process of (d) Cu and (e) Cu−$Bi_{0.1}$ on carbon paper from Cu-Phen and Bi-Phen ink mixture.

facilitates C−N bond formation. By leveraging density functional theory (DFT) calculations, we also elucidated the thermodynamics and kinetics, demonstrating that alloying Cu with Bi enhances urea selectivity through several critical factors: (1) securing *CO binding, (2) efficiently enhancing *NO_2 binding, (3) favoring the subsequent C−N coupling step, and (4) optimizing *$CONO_2$ binding. By doing so, we aim to contribute to the development of a sustainable and economically viable route for the production of 'green urea', aligning with the global imperative for sustainable development. This work not only deepens our understanding of the catalytic mechanisms underlying urea synthesis but also establishes a foundational blueprint for designing highly selective and efficient electrocatalysts.

RESULTS AND DISCUSSION

The supported ultrafine Cu-M (M = Bi, In, and Pb; with a Cu:M molar ratio of 10:1) nanoalloys were synthesized using a modified electrodeposition method by first complexing the metal cations with 1,10-phenanthroline ('Phen'), as illustrated in Figure 2a. We anticipated that the metal complexation with Phen should regulate the electrochemical reduction kinetics, which should enable the synthesis of finer and more controlled nanoparticles. To obtain the Cu-$M_{0.1}$ nanoalloy, ink mixtures containing Cu-Phen and M-Phen were loaded onto hydrophobic carbon fiber papers. Subsequently, electrochemical reduction was carried out at −1.5 V vs RHE in 0.5 M KNO_3 for 1 h. The electrodeposited carbon fiber paper was thoroughly washed with deionized water and alcohol to ensure electrode cleanliness. Detailed experimental procedures for catalyst preparation can be found in the Method section of the Supporting Information (SI).

To avoid any experimental error arising from incomplete complexation of the metal ions, we first investigated the metal ratio of the catalysts (see Tables S1 and S2 in the SI). The actual molar ratio between Cu and M has been found close to the theoretical molar ratio with less than 10% deviation. We then employed in situ transmission electron microscopy (TEM) to visualize the electrodeposition process on carbon fiber paper. As shown in Figure 2b, the in situ TEM investigation 'recorded' the rapid formation of uniformly dispersed ultrafine Cu−$Bi_{0.1}$ nanoparticles upon the application of an external voltage. Continuous formation of these ultrafine nanoparticles was observed during the first 15 s. Thereafter, the morphology of the nanoparticles remained unchanged, with no further aggregation or increase in size noted. The high-resolution TEM (HRTEM) image in Figure 2c reveals a set of lattice fringes with a *d*-spacing of 2.27 Å, which is greater than

https://doi.org/10.1021/acscatal.5c01960
ACS Catal. 2025, 15, 8966−8978

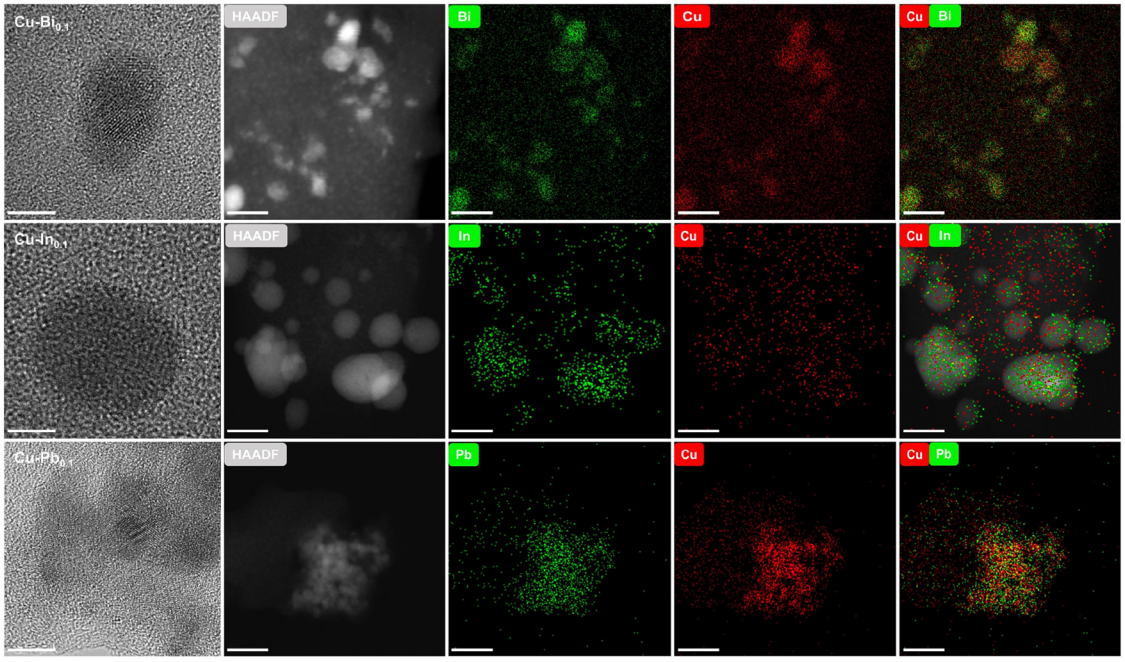

Figure 3. HRTEM images of Cu−$Bi_{0.1}$, Cu−$In_{0.1}$, and Cu−$Pb_{0.1}$, with a scale bar of 5 nm, and the corresponding TEM-EDX mapping with a scale bar of 20 nm.

the lattice spacing of pure Cu(111) (d = 2.10 Å). This expansion is primarily caused by the substitution of a portion of the Cu atoms with Bi, indicating the formation of nanoparticles that are not pure Cu. We have also employed in situ Raman spectroscopy to study the electrodeposition process of Cu and Cu−$Bi_{0.1}$ on carbon paper (Figure 2d,e). The Raman peaks characteristic of Phen completely disappeared within 60 s, inferring the formation of nanoalloys in a reduced form during the electrodeposition process.

The HRTEM images reveal that all Cu-$M_{0.1}$ samples exhibit a sphere-like morphology, having an average diameter of approximately 10 nm (Figure 3). In contrast, the Cu−$Bi_{0.1}$(no-Phen) sample synthesized without using the Phen-mediated approach resulted in much larger nanoparticles with a size of around 50 nm (refer to Figure S1). This observation suggests that the modified 'Phen-mediated' electrodeposition method provides much better control and reduction in nanoparticle size. Additionally, the corresponding EDX spectroscopy mapping confirms the uniform distribution of Cu, Bi, In, and Pb throughout the samples.

Our substrate-free cyclic voltammetry (CV) measurements (Figure S2) confirmed a metallic Cu(0) valence state within the operation voltage range of interest between −0.8 and −1.4 V vs RHE. However, due to the ultrafine sizes of these nanoalloys, they are prone to oxidation once the applied voltage is removed after electrodeposition. Conventional ex-situ measurements may not be able to accurately reflect the chemical information about these supported Cu-M nanoalloys, especially under working electrochemical conditions. Our ex-situ investigations, using X-ray photoelectron spectroscopy (Figures S3−S5), X-ray absorption near edge spectroscopy (Figure S6), extended X-ray absorption fine structure spectroscopy (Figures S7−S9), and powder X-ray diffraction (Figures S10−S13), all show the presence of copper oxides species.

The electrochemical properties of urea synthesis from NO_3^- and CO_2 were assessed using the potentiostatic method in an H-cell reactor. The anodic and cathodic chambers were separated by a Nafion 117 membrane. The measurements were conducted under ambient temperature (24.0 ± 0.5 °C) and pressure. Throughout the reaction process, high-purity CO_2 was continuously supplied to the cathodic chamber electrolyte (0.1 M KNO_3). The flow rate of CO_2 was maintained at 50 sccm. Gas chromatography (GC) was utilized to quantify the products in the gas phase. The majority of the products are NO_2^-, NH_3, CO, H_2, and urea. Urea, ammonia, and nitrite were quantified using the modified DAMO-TSC method[25,26] and ultrahigh-performance liquid chromatography,[1,27] the indophenol blue method,[28] and the N-(1-naphthyl)-ethylenediamine dihydrochloride method,[29] respectively.

Figure 4a−d depicts the FEs of the major products at various working potentials ranging from −0.8 to −1.4 V vs RHE for Cu, Cu−$Bi_{0.1}$, Cu−$In_{0.1}$, and Cu−$Pb_{0.1}$ catalysts. The FE_{urea} for all catalysts exhibits a volcano-shaped distribution, with the highest selectivity observed at −1.0 V vs RHE. Notably, the Cu−$Bi_{0.1}$ catalyst demonstrates the highest selectivity, with an impressive FE_{urea} of 89.4%, surpassing most reported catalysts. Cu−$In_{0.1}$ and Cu−$Pb_{0.1}$ exhibit lower FE_{urea} values of 78.6 and 62.1%. In comparison, it is worth mentioning that the FE_{urea} over Cu−$Bi_{0.1}$ is more than doubled that over the pristine Cu catalyst at −1.0 V vs RHE (cf. FE_{urea} of 41.5%, Figure 4e). These notable differences indicate that the doping of Bi, In, and Pb effectively enhances the selectivity of urea during the electrochemical coreduction of nitrate and CO_2. Furthermore, Cu−$Bi_{0.1}$ outperforms the analogous Cu−$Bi_{0.1}$(no-Phen) catalyst, demonstrating a much higher selectivity by around 30% in FE_{urea} (Figure S14), highlighting the impact of using finer nanoalloys for catalysis. Additionally, Cu−$Bi_{0.1}$ achieves an impressive urea yield of 586.87 $\mu g\ h^{-1}\ mg_{cat}^{-1}$ at −1.2 V vs RHE, highlighting its potential for further commercialization and development, such as adopting stack cells for large-scale urea production.

It is worth noting that the Cu-M samples exhibit notably lower FE_{NO2-} and FE_{NH3} compared to the pristine Cu catalyst,

https://doi.org/10.1021/acscatal.5c01960
ACS Catal. 2025, 15, 8966−8978

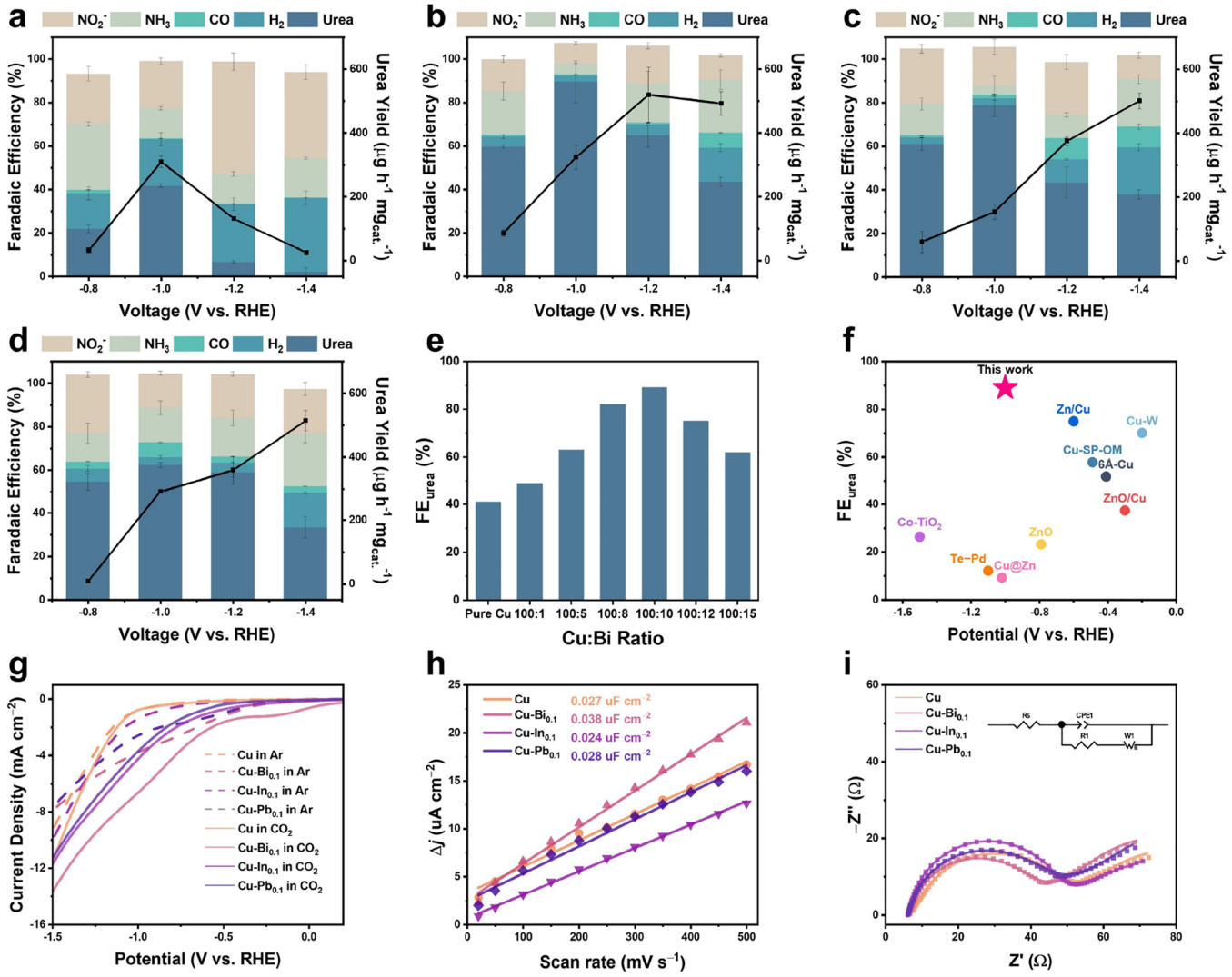

Figure 4. Product distribution from the electrochemical reduction of flowing CO_2 in 0.1 M KNO_3 at various potentials over (a) Cu, (b) Cu−$Bi_{0.1}$, (c) Cu−$In_{0.1}$, and (d) Cu−$Pb_{0.1}$. (e) FE_{urea} of Cu−Bi_x with different Cu: Bi ratios, ranging from 1:0.01 to 1:0.15, at an applied voltage of −1.0 V vs RHE. (f) Comparison of the results of this work with recently published electrocatalysts in terms of applied potential and FE_{urea}. (g) LSV curves of Cu and Cu-M using CO_2 or Ar saturated electrolyte. (h) Quasi-linear relationship between the current densities at 0.4 V vs RHE of different samples and scan rates. (i) Nyquist plots of Cu and Cu-M obtained at 0 V vs open-circuit potential, covering a frequency range from 0.01 Hz to 100 kHz with an amplitude of 5 mV. The inset shows the equivalent electrical circuit used for the simulation analysis.

indicating that more NO_2^- reduction intermediates are utilized for the subsequent formation of urea.[10] Throughout the electrocatalysis process, only CO and H_2 were observed as the gas products. The FE_{H2} of Cu reaches its highest value of 34.1% at −1.4 V vs RHE, which is significantly higher than the FE_{H2} values of the Cu-M samples at all the investigated potentials. We also conducted GC and NMR measurements to provide a comprehensive product analysis. Our results indicate that CO is the sole detected carbonaceous gas product, with a concentration below 20 ppm, corresponding to a FE_{CO} of 1.66% (Figure S15). For liquid-phase analysis, we performed ^{13}C NMR measurements and detected nil carbon-containing liquid products. Control experiments have been done to confirm the origin of carbon and nitrogen in the product urea (Figure S16).

To determine the optimal Cu-to-Bi ratio for urea electrosynthesis, we conducted measurements on various Cu−Bi_x samples with ratios ranging from 100:1 to 100:15 at −1.0 V vs RHE (Figure 4e). The FE_{urea} for the Cu−Bi_x catalysts exhibits a volcano-shaped distribution, with Cu−$Bi_{0.1}$ demonstrating the highest FE_{urea}. Importantly, all three Cu-M catalysts exhibit superior FE_{urea} compared to the pristine Cu catalyst. A comprehensive comparison with recently reported catalytic systems is summarized in Figure 4f, highlighting the much superior properties exhibited by Cu−$Bi_{0.1}$.

Figure 4g shows the linear sweep voltammetry (LSV) curves of Cu, Cu−$Bi_{0.1}$, Cu−$In_{0.1}$, and Cu−$Pb_{0.1}$ catalysts. Upon switching from Ar to CO_2 atmosphere, an increase in the reduction current density is observed for all four catalysts within the potential range of 0.2 to −1.5 V vs RHE. This indicates that the presence of CO_2 enhances the catalyst's sensitivity and effectively suppresses the competing hydrogen evolution reaction.[9] To investigate the electrochemically active surface area, CV measurements at different scan rates were conducted (Figures S17−S20). Figure 4h shows that Cu−$Bi_{0.1}$ exhibits the highest electrochemical double-layer capacitance (C_{dl}) of 0.038 μF cm^{-2} among the four catalysts. In contrast, Cu, Cu−$Pb_{0.1}$, and Cu−$In_{0.1}$ demonstrate comparable C_{dl}

https://doi.org/10.1021/acscatal.5c01960
ACS Catal. 2025, 15, 8966−8978

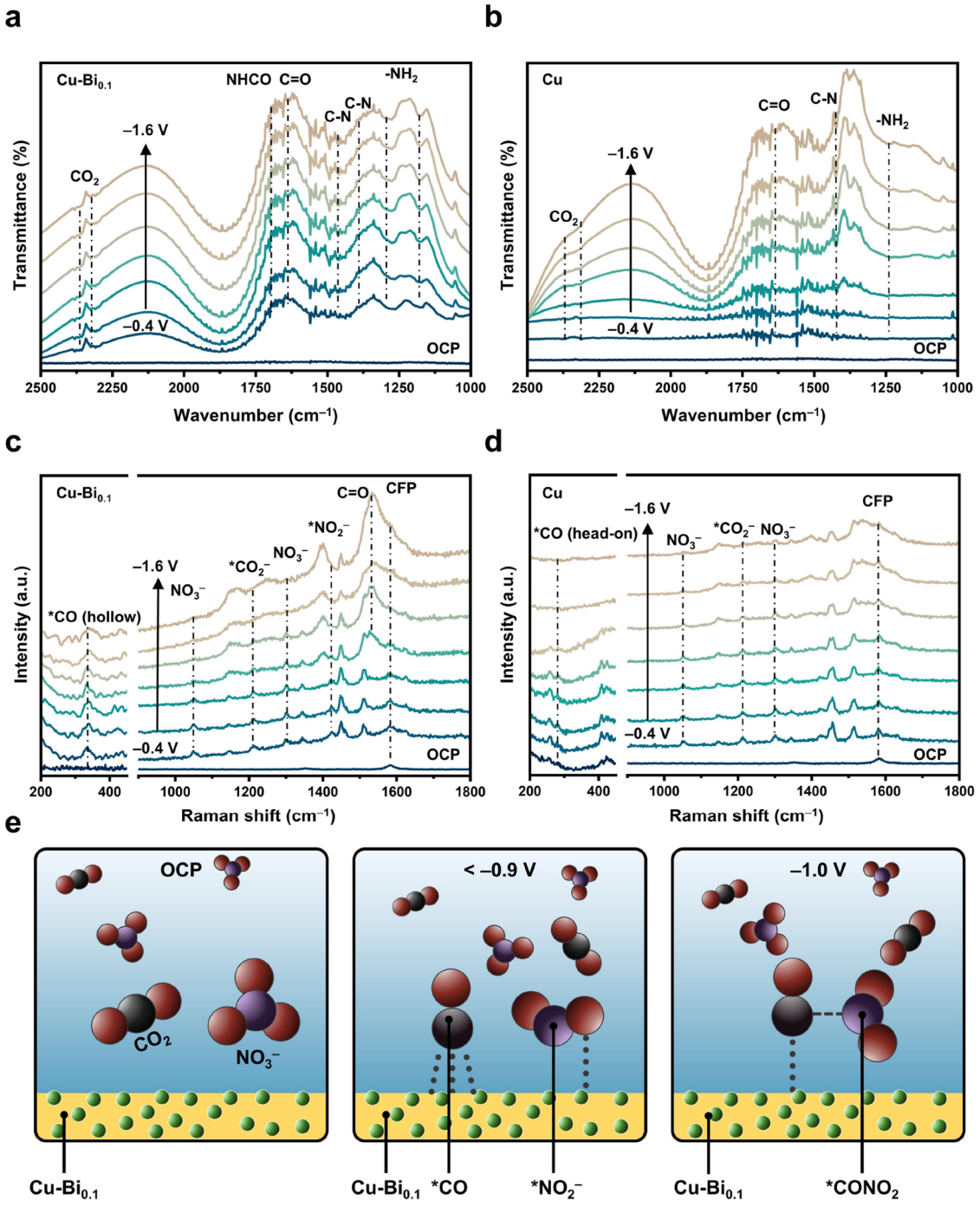

Figure 5. *Operando* ATR-FTIR spectroscopy measurements of (a) Cu−$Bi_{0.1}$ and (b) Cu, in 0.1 M KNO_3 with flowing CO_2 under potentials from −0.4 to −1.6 V vs RHE. *Operando* Raman spectroscopy measurements of (c) Cu−$Bi_{0.1}$ and (d) Cu, in 0.1 M KNO_3 with flowing CO_2 under potentials ranging from −0.4 to −1.6 V vs RHE. (e) Schematic illustration highlighting some key findings observed from the *operando* Raman spectroscopy study. Carbon fiber paper is abbreviated as CFP.

values of approximately 0.027 μF cm^{-2}. This discrepancy suggests that Cu−$Bi_{0.1}$ possesses more exposed active sites, which should lead to facilitated adsorption and activation of CO_2 and NO_3^-.[30,31]

Electrochemical impedance spectroscopy was utilized to investigate the electron/ion transfer kinetics during the electrocatalytic process. The Nyquist plots are shown in Figure 4i. The circuit model includes the electrolyte resistance (R_s), charge transfer resistance (R_{ct}), constant phase element (CPE), and Warburg impedance associated with potassium ion diffusion (W). All four catalysts demonstrated similar R_s values of approximately 6.5 Ω, indicating that they exhibit comparable catalytic environments.[32] Among the catalysts, Cu−$Bi_{0.1}$ exhibited the lowest R_{ct} value, suggesting that the coreduction of CO_2 and NO_3^- experiences the least resistance at the electrolyte/catalyst interface.[33] This result implies that Cu−$Bi_{0.1}$ possesses more favorable electron/ion transfer kinetics during the electrocatalytic process.

We subsequently assessed the stability of Cu−$Bi_{0.1}$ through a long-time measurement at −1.1 V vs RHE in CO_2-saturated

https://doi.org/10.1021/acscatal.5c01960
ACS Catal. 2025, 15, 8966−8978

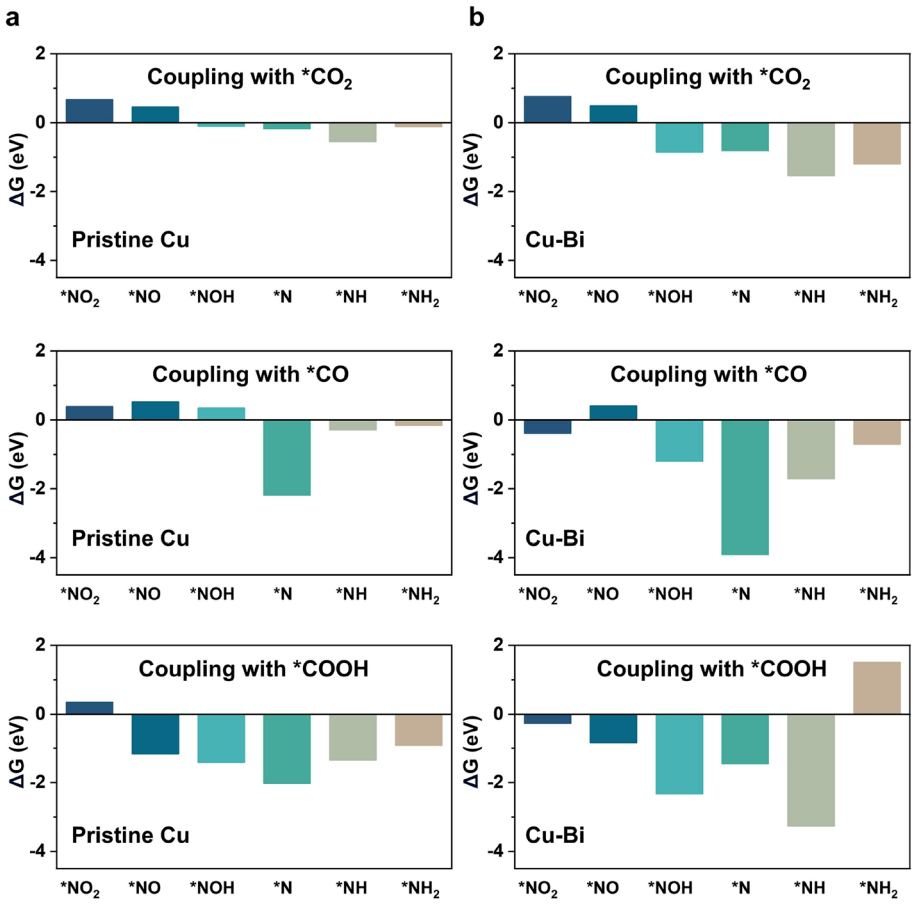

Figure 6. Calculated Gibbs free energy changes (ΔG) for 18 C−N coupling pathways on (a) pristine Cu (111) and (b) Bi-doped Cu (111) surfaces.

0.1 M KNO_3 for six consecutive reaction cycles (2 h for each cycle). As illustrated in Figure S21a, the FE_{urea} of Cu−$Bi_{0.1}$ remained within 85 and 90%, indicating high catalytic stability. The urea yield fluctuated regularly between 310 and 373 $\mu g\ h^{-1}\ mg_{cat}^{-1}$, with a slight variation of 63 $\mu g\ h^{-1}\ mg_{cat}^{-1}$. This narrow-range fluctuation pattern aligned with the stable trend observed in FE_{urea}. The current density curves in Figure S21b also echoed these results. The experimental data confirm that the catalytic system has been effectively preserved under continuous electrochemical operation. We then conducted a series of postreaction characterizations to further assess the structural and chemical stability of the Cu−$Bi_{0.1}$ sample. As shown in Figure S22, the HRTEM confirmed that the spherical nanostructure of the catalyst was maintained throughout the reaction process with an average diameter of ∼10 nm. EDX elemental mapping verified the homogeneous distribution of Bi species within the Cu domain. In addition, postreaction XPS (Figure S23) and XRD (Figure S24) analyses both reveal no significant alterations compared to the as-prepared state.

Furthermore, to address concerns regarding potential catalyst leaching, we performed ICP-OES analysis of the electrolyte after six electrocatalytic cycles. As shown in Table S3, nil Bi or Cu was detected, confirming that catalyst leaching was negligible under the experimental conditions. This result reinforces the stability of the Cu−$Bi_{0.1}$ catalyst during prolonged electrochemical operation.

To investigate the reaction mechanism, *operando* attenuated total reflectance Fourier-transform infrared spectroscopy (ATR-FTIR) was performed on Cu−$Bi_{0.1}$ and Cu catalysts. The *operando* ATR-FTIR spectra were collected in the range of 1000−2500 cm^{-1} under the negative scan mode, ranging from −0.4 to−1.6 V vs RHE, as shown in Figure 5a,b. The IR signals at 1175, 1295, and 1625 cm^{-1} can be attributed to the rocking, wagging, and bending modes of−NH_2 in urea.[18,34,35] In addition to the −NH_2 bands, characteristic IR signals of the C−N bond were also observed on the catalysts when negative potentials were applied, showing at 1400, 1420, and 1450 cm^{-1}.[36] Specifically, the wavenumbers of the C−N bond signals slightly differed between Cu (1420 cm^{-1}; coordinated urea[37]) and Cu−$Bi_{0.1}$ (1450 cm^{-1}; physisorbed urea[38]). This difference can be attributed to a stronger binding of urea on the Cu surface when compared with that on the Cu−$Bi_{0.1}$ surface, which can potentially promote catalysis by facilitating a more rapid release of the urea molecule once it is formed. IR peaks characteristic of C═O was found at 1640 cm^{-1} over both catalysts.[36,39] Furthermore, we observed an IR peak at 1694 cm^{-1} only on Cu−$Bi_{0.1}$, which can be attributed to the C═O stretch in *CONH.[40] The observation of this peak can suggest a stronger stabilization of *CONH on the catalyst surface, which is a key intermediate after the C−N coupling step in the urea synthesis process.[41]

To provide more evidence on the detection of these intermediate species, we have conducted additional in situ ATR-FTIR measurements using isotopically labeled $K^{14}NO_3$ and $K^{15}NO_3$ as the nitrogen source, as shown in Figure S25. Upon replacing the original 0.1 M $K^{14}NO_3$ electrolyte with 0.1 M $K^{15}NO_3$, the characteristic C−N stretching peak exhibits a redshift of ∼27 cm^{-1}, consistent with the kinetic isotope

https://doi.org/10.1021/acscatal.5c01960
ACS Catal. 2025, 15, 8966−8978

effect.[42] In contrast, the C═O stretching peak at 1640 cm^{-1} remains unchanged, suggesting that the observed shift is specific to the C−N bond formation. This result provides strong evidence that the C−N coupling reaction occurs on the catalyst surface and verifies that the N element in the electrosynthesized urea originates from the electrolyte.

Operando Raman spectroscopy was employed to further investigate the enhanced urea selectivity exhibited by Cu−$Bi_{0.1}$ compared to pristine Cu (Figure 5c,d). Cu displayed a Raman peak at 282 cm^{-1}, characteristic of head-on *CO adsorption on the catalyst surface.[43] In contrast, Cu−$Bi_{0.1}$ exhibited a peak at 330 cm^{-1}, characteristic of adsorbed hollow *CO species on the surface.[44] The *CO signals became stronger as the applied potential became more negative, peaking at −1.0 V vs RHE. We also observed a Raman signal at 1211 cm^{-1} corresponding to the symmetric mode of CO_2^-.[45] The Raman signals at 1049 and 1300 cm^{-1} can be attributed to the vibrations of free NO_3^- and bidentate adsorbed NO_3^- species.[46] These NO_3^- signals began to decrease at more negative potentials, consistent with the facile electrochemical reduction of NO_3^-. Some Raman peaks characteristic of adsorbate *CO and NO_3^- reduction products were also observed, including NH_3 in both Cu and Cu−$Bi_{0.1}$ and bridging *NO_2 at 1428 cm^{-1},[9] which was only found in Cu−$Bi_{0.1}$.

Excitingly, we observed a notable dynamic change in the set of Raman peaks in Cu−$Bi_{0.1}$. At more negative potentials, along with the fading of *NO_2 and *CO (completely disappeared at −1.0 V vs RHE), we noted a gradual emergence of a Raman signal at 1540 cm^{-1}, which is characteristic of the C═O stretching of urea.[27] It should be noted that this dynamic change was not noticeable in Cu, suggesting that Cu−$Bi_{0.1}$ can better promote the electrochemical coupling of surface *NO_2 and *CO. Figure 5e highlights some key findings observed from the *operando* Raman spectroscopy investigation. This intriguing finding provides insights into the reaction mechanism that contributes to the superior FE_{urea} observed in Cu−$Bi_{0.1}$ during the electrochemical coreduction of CO_2 and nitrate.

Density function theory (DFT) calculations were conducted to elucidate the mechanism underlying the superior selectivity observed in Cu-M catalysts in the electrosynthesis of urea. Given the complexity of urea synthesis, which involves multiple plausible C−N coupling pathways, we systematically examined 18 C−N coupling pathways on pristine Cu and Bi-doped Cu(111) surfaces, considering *CO_2, *CO and *COOH as the C sources and *NO_2, *NO, *NOH, *N, *NH, *NH_2 as the N sources (Figure 6). Our results indicate that, compared to pristine Cu, the Bi-doped Cu surface can effectively promote the C−N coupling by shifting thermodynamically unfavorable reactions (Gibbs free energy changes, $\Delta G > 0$) into favorable reactions ($\Delta G < 0$) or further reducing the negative ΔG. Among the examined pathways, the coupling between *CO and *N exhibits the most exergonic, exhibiting ΔG of −3.90 eV. It is noteworthy that our *operando* studies provide compelling evidence for two key observations: (1) a consistently enhanced *CO adsorption, and (2) a decrease of *NO_2 accompanied by a concurrent increase of C−N, likely indicating the direct consumption of *CO and *NO_2 for C−N bond formation over Cu−$Bi_{0.1}$ surface. These findings align well with the proposed mechanism in previous studies.[47−49] Therefore, we adopt the coupling between *NO_2 and *CO to form *$CONO_2$ as the initial C−N bond formation step in constructing the postulated reaction pathway.

As shown in Figure 7, Bi doping significantly enhances *NO_2 adsorption by lowering the energy for *NO_3 → *NO_2

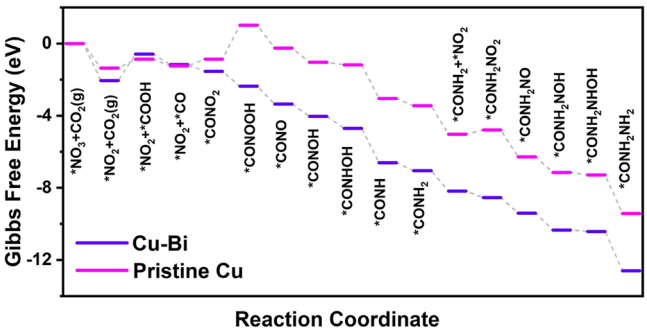

Figure 7. Gibbs free energy diagram for urea production on pristine Cu (111) and Bi-doped Cu (111) surfaces.

conversion from −1.36 to −2.05 eV, thereby facilitating C−N coupling. This effect is evident from the Gibbs free energy changes in the first and second C−N bond formation steps. For the initial coupling step (*CO + *NO_2 → *$CONO_2$), Bi-doping reduces the Gibbs free energy change from 0.38 eV on pristine Cu (111) to −0.38 eV on Bi-doped Cu (111), transforming the reaction from nonspontaneous to spontaneous. Similarly, for the second coupling step, Bi-doped Cu (111) reduces the Gibbs free energy change to −0.36 eV, compared to 0.23 eV on pristine Cu, further confirming its role in promoting C−N bond formation. Beyond facilitating C−N coupling, Bi doping stabilizes key intermediates and reduces the energy barriers for subsequent hydrogenation steps (e.g., *$CONO_2$ → *CONOH → *CONH → *$CONH_2$). Notably, Bi-doping shifts the potential determining step (PDS) from the hydroxylation of *$CONO_2$ on pristine Cu (111) to *COOH formation on the modified surface, effectively lowering the energy barrier from 1.88 to 1.46 eV. This step is the only one involving a positive ΔG, while the rest of the reaction pathway remains thermodynamically favorable, indicating a significantly facilitated urea production process. Overall, these results collectively demonstrate that Bi-doping enhances urea formation on Cu (111) both thermodynamically and kinetically.

CONCLUSIONS

In this study, we first presented a robust protocol for synthesizing ultrafine nanoparticles for both pure metals and bimetallic alloys, offering high control over particle size and dopant distribution. The ultrafine nanoparticles generally enhance urea selectivity through facilitated intermediate adsorption and activation, providing a robust guideline for designing high-performance catalysts for urea electrosynthesis. Specifically, our Cu−$Bi_{0.1}$ sample achieves a high FE_{urea} of 89.4% at −1.0 V vs RHE. This showcases a notable enhancement in catalytic properties through a combination of 'size effect' and 'dopant effect' modifications.

Integrated *operando* spectroscopic evidence has revealed the preferential stabilization of the *CO and *NO_2 intermediates on the Cu−$Bi_{0.1}$ surface. Importantly, this research offers a promising integrated theory-experiment approach to guide the selection of *new-generation* Cu-based nanoalloys for the electrochemical coreduction of CO_2 and nitrate to produce urea selectively. It is anticipated that this rational design

https://doi.org/10.1021/acscatal.5c01960
ACS Catal. 2025, 15, 8966−8978

methodology can be transferred to the development of other high-performance catalytic systems.

EXPERIMENTAL METHODS

Chemicals. Copper(II) chloride dihydrate ($CuCl_2{\cdot}2H_2O$; ≥99%); bismuth nitrate pentahydrate ($Bi(NO_3)_3{\cdot}5H_2O$; ≥99.0%); nickel(II) nitrate hexahydrate ($Ni(NO_3)_2{\cdot}6H_2O$; 99.99%); lead(II) nitrate ($Pb(NO_3)_2$; ≥99.0%); 1,10-phenanthroline ($C_{12}H_8N_2$; ≥99.0%; 'Phen'); Nafion 117 solution (5 wt %); isopropyl alcohol ($(CH_3)_2CHOH$; 99.7%); sodium citrate ($C_6H_5Na_3O_7$; ≥99.0%); potassium nitrate (KNO_3; ≥99.0%); sulfuric acid (H_2SO_4; 98%); phosphoric acid (H_3PO_4; 85%); salicylic acid (2-(HO)$C_6H_4CO_2H$; ≥99.0%); ferric chloride ($FeCl_3$; ≥99.9%) were purchased from Sigma-Aldrich. Thiosemicarbazide (CH_5N_3S; ≥98.0%); diacetyl monoxime ($C_4H_7NO_2$; ≥98.0%); urea (CH_4N_2O; ≥99.0%); N-(1-Naphthyl)ethylenediamine dihydrochloride ($C_{12}H_{14}N_2{\cdot}2HCl$; ≥99.0%) were purchased from TCI. Sodium nitroferricyanide dihydrate ($C_5H_4FeN_6Na_2O_3$; ≥98.5%); and sulfanilamide ($C_6H_8N_2O_2S$; ≥99.8%) were purchased from Shanghai Yuanye. All reagents were used as purchased and used without any further purification.

Synthesis of Metal-Phen Precursor. The synthesis of the precursors was conducted according to the previous literature.[50] To prepare 'Cu-Phen', 0.5 mmol of copper(II) chloride dihydrate and 1.0 mmol of 1,10-phenanthroline ('Phen') were added to a flask containing 30 mL isopropanol. The mixture was then heated to 80 °C and kept stirring overnight. After thorough evaporation of isopropanol, the green powder was obtained. To remove free Cu^{2+} and Phen, the powder was washed with a mixture of water and isopropanol several times. In synthesizing Cu−$Bi_{0.1}$-Phen, Cu−$In_{0.1}$-Phen, and Cu−$Pb_{0.1}$-Phen precursors, the second metal-Phen was physically mixed with the Cu-Phen to form an ink mixture.

Working Electrode Preparation. For the preparation of the precursor ink, 10 mg of Cu-$M_{0.1}$-Phen was mixed with 900 μL of isopropanol and 100 μL of 5 wt % Nafion solution. After sonication for 30 min, a homogeneously dispersed ink with a concentration of 10 mg mL^{-1} was obtained. In the preparation of the working electrode, we deposited 50 μL (equivalent to 0.5 mg) of the Cu-$M_{0.1}$-Phen ink onto carbon paper. Following this, we proceeded to dry the electrode at 60 °C for 8 h to ensure all isopropanol was removed from the working electrode.

Controlled Electrodeposition. We conducted the electrodeposition in a standard H-cell electrochemical reactor equipped with a three-electrode configuration. The reference electrode was KCl-saturated Ag/AgCl, while 1 × 1 cm^2 Pt mesh was used as the counter electrode. 0.5 M KNO_3 solution was used as the electrolyte for the electrodeposition process. Under controlled conditions, the electrodeposition treatment was carried out for 1 h at a potential of −1.5 V vs RHE. Throughout this process, Phen was eliminated, resulting in the formation of Cu-$M_{0.1}$ nanoalloy.

Electrochemical Measurements. A standard three-electrode H-cell reactor was employed to conduct the electrocatalytic measurements. The electrochemical measurements were conducted by CHI 760E Electrochemical Workstation. KCl-saturated Ag/AgCl and 1 × 1 cm^2 Pt foil were used as the reference electrode and counter electrode, respectively. A Nafion membrane was employed to separate the cathode and anode chambers of the H-Cell. Each chamber was filled with 50 mL of 0.1 M KNO_3 solution, serving as the electrolyte for the electrochemical experiment. Before initiating the electrochemical experiment, the cathode chamber underwent a pretreatment step. To ensure the CO_2 atmosphere during the whole reaction process, a high-purity CO_2 gas (99.999%) was purged into the cathode chamber via bubbling at a controlled flow rate of 50 sccm for 30 min. This purging process was continued until the pretreatment procedure was completed. In addition, we also set the stirring at a constant rate at 400 rpm to ensure the electrolyte and reactants exchange efficiency. All potentials were converted to the reference scale of the reversible hydrogen electrode (RHE) using the following equation:

$$E_{(\text{vs RHE})} = E_{(\text{vs Ag/AgCl})} + E^0{}_{\text{Ag/AgCl}} + 0.0591 \times \text{pH} \quad (1)$$

In the given equation, $E_{(\text{vs RHE})}$ represents the potential in V vs RHE. $E_{(\text{vs Ag/AgCl})}$ denotes the potential measured for the reference electrode Ag/AgCl. Furthermore, $E^0{}_{\text{Ag/AgCl}}$ corresponds to the potential of the Ag/AgCl reference electrode, which is determined in an H_2-saturated 0.1 M $HClO_4$ solution with a pH of 1.1.[10]

The electrochemical active surface area of the electrocatalysts was determined by measuring the electrochemical double-layer capacitance (C_{dl}). To measure C_{dl}, we selected a potential window ranging from 0.3 to 0.5 V vs RHE where no Faradaic reactions were observed. CV measurements were recorded at different scan rates. The difference between the anodic and cathodic currents at 0.4 V vs RHE was plotted against the corresponding scan rates. The resulting linear slope of this plot corresponds to twice the value of the C_{dl}. Nafion 117 membrane was used as the proton exchange membrane to separate the cathode and anode compartments. CO_2-saturated KNO_3 was used as the electrolyte.

Quantitative Analysis of Gas and Liquid-Phase Products. The gas products were analyzed by gas chromatography (GC) equipped with both a flame ionization detector (FID) and a thermal conductivity detector (TCD). We used high-purity nitrogen gas (99.99%, Linde) as the carrier gas. To determine the CO concentration, we used an FID with a TDX-01 column for CO measurement and a TCD with 6-foot MolSieve 5A mesh columns to detect the concentration of H_2. Furthermore, the column oven temperature was set at 70 °C. The relative liquid products were detected by using ^{13}C NMR (Bruker Avance NEO 500 NMR Spectrometer).

Faradaic Efficiency and Yield Calculation. The average yield rate of urea was calculated using the following equation:

$$\text{Yield}_{\text{urea}} = \frac{C_{\text{urea}} \times V}{t \times m} \quad (2)$$

where C_{urea} is the measured concentration of urea (μg mL^{-1}), V is the total volume of cathode electrolyte (mL), t is time (h) for electrocatalysis during the time and m is the loadings weight of catalysts (mg).

The FE for liquid products was calculated using the following equation:

$$\text{FE} = \frac{N \times F \times m}{Q} \quad (3)$$

where N is the number of electron transfers, F is the Faraday's constant (96,485.3 C mol^{-1}), m is the total moles of products and Q is the total charge passed through.

https://doi.org/10.1021/acscatal.5c01960
ACS Catal. 2025, 15, 8966−8978

The FE of gas products was calculated using the following formula:

$$FE_{gas}(\%) = \frac{zFG\rho}{V_m \times i_{total}} \times 100 \quad (4)$$

where Z is the number of electrons transferred, F is Faraday's constant, G is the flow rate of gas (20 sccm), ρ is the molar fraction of the product, V_m is the standard gas molar volume (24 L mol^{-1}), and i_{total} is the total current.

Urea Measurement by the Modified DAMO-TSC Method. An acid-ferric solution was prepared by combining 100 mL of concentrated phosphoric acid, 300 mL of concentrated sulfuric acid, 600 mL of deionized water, and 100 mg of ferric chloride. To prepare the DAMO-TSC solution, 5 g of DAMO and 100 mg of TSC were mixed and dissolved in 1000 mL of deionized water. After the electrocatalytic measurements, a subsequent step involved the mixing of 1 mL of the electrolyte, 2 mL of the acid-ferric solution, and 1 mL of the DAMO-TSC solution. The resulting mixture was boiled in a metal bath for 30 min. After cooling down to room temperature, the absorbance of the solution was measured at a wavelength of 518 nm using a UV−vis spectrophotometer. The concentration-absorbance calibration curve was obtained by plotting the absorbance of standard solutions, as illustrated in Figure S26.

Urea Measurement by UPLC. Urea was quantified using ultrahigh-performance liquid chromatography (UPLC) on an Agilent 1290 Infinity II system equipment with a Polaris NH_2 column (4.6 mm × 250 mm). An acetonitrile−water mobile phase (80:20) was used at a flow rate of 0.1 mL min^{-1}, and urea absorbance was obtained at 195 nm using a diode array detector. Before the UPLC analysis, the electrolyte was filtered through a 0.22 μm membrane to eliminate potential contaminants. A calibration curve relating urea concentration to absorbance was generated using a standard solution (Figure S27) and independently validated.

Ammonia Measurement. We utilized the indophenol blue method to determine the concentration of ammonia.[28] This involved adding 2 mL of the sample electrolyte to 2 mL of 1.0 M NaOH solution containing 5 wt % salicylic acid, 5 wt % sodium citrate, 1 mL of 0.05 M NaClO, and 0.2 mL of 1 wt % sodium nitroferricyanide. After keeping the mixture at room temperature for 2 h, the absorbance spectrum was collected at 657 nm using a UV−vis spectrophotometer. The calibration curve of concentration-absorbance was plotted with the absorbance of standard ammonia solutions, as shown in Figure S28.

Nitrite Measurement. We employed a modified spectrophotometric method using N-(1-naphthyl)-ethylenediamine dihydrochloride to determine the concentration of nitrite.[51] After the electrocatalysis 2 mL of the electrolyte was mixed with 0.1 mL of a 4-aminobenzenesulfonamide aqueous solution, followed by a reaction for 8 min. Subsequently, 0.1 mL of N-(1-naphthyl) ethylenediamine dihydrochloride aqueous solution, with a concentration of 1 g L^{-1}, was added to the above mixture. After the further reaction for 10 min in the dark, the absorbance was acquired at 540 nm using a UV−vis spectrophotometer. The calibration curve of concentration-absorbance was plotted with the absorbance of standard $NaNO_2$ solutions, as shown in Figure S29.

XAFS Measurement. X-ray absorption spectroscopy data using the fluorescence mode was collected on Beamline 01C1 at Taiwan Light Source. For energy calibration, a Cu foil was employed, and the fluorescence X-ray intensity was monitored using a Lytle-type detector. To calibrate the acquired X-ray absorption fine structure data, we utilized the Athena software to calibrate the background, pre-edge line, and postedge line of the X-ray absorption spectra.[52] Additionally, the absorption data was Fourier transformed using a k-range of 3.0 to 11 Å^{-1} and an R-range of 1.0 to 3.5 Å^{-1}. To calculate the simulated scattering paths, models of Cu, CuO, and the actual samples were used. The parameters, including coordination number (CN), bond length (R), Debye−Waller factor (δ^2), and standard potential (E_0) shift (ΔE_0), were fitted with partial constraints to ensure the accuracy of results.

Operando Raman Spectroscopy. *Operando* Raman measurements were performed using a three-electrode flow cell acquired from Gaoss Union. The setup included a carbon paper working electrode, a Pt mesh counter electrode, and an Ag/AgCl reference electrode immersed in saturated KCl. Electrochemical assessments were executed in a CO_2-saturated 0.1 M KNO_3 electrolyte employing the potentiostat method at −1.0 V vs RHE. High-purity CO_2 gas was consistently introduced into the electrolyte at a flow rate of 50 sccm regulated by a mass flow controller. The electrolyte circulated through the cell continuously at a rate of 1 mL min^{-1}. Raman spectroscopy was conducted via a Renishaw Micro-Raman Spectroscopy System with an Intertec λ = 532 nm laser source operating at 5% power. The Raman probe was precisely targeted at the electrode/electrolyte interface via a quartz window.

OPERANDO ATR-FTIR SPECTROSCOPY

For *operando* ATR-FTIR measurements, a THERMO Nicolet 6700 spectrometer equipped with a liquid nitrogen-cooled MCT detector was used. The measurements were conducted with an applied voltage set at −1.0 V vs RHE. A glassy carbon electrode coated with a catalyst (1 mg cm^{-2}) was used as the working electrode. An Ag/AgCl electrode was used as the reference electrode, while a carbon electrode functioned as the counter electrode. Furthermore, a Si facet crystal positioned at an incident angle of 60° was employed as the reflective element. The electrolyte used was a 0.1 M CO_2-saturated KNO_3 solution. The isotope labeling experiment is consistent with the above results except that $K^{14}NO_3$ was replaced by $K^{15}NO_3$.

Computational Methods. The density functional theory (DFT) calculations were performed using the projector-augmented wave method as implemented in the Vienna Ab initio Simulation Package (VASP). The generalized gradient approximation (GGA) with the Perdew−Burke−Ernzerhof (PBE) exchange-correlation functional was used. A uniform 6 × 6 × 6 k-mesh grid in the Brillouin zone was employed to optimize the crystal structure of bulk Cu. The Cu slab model with five atomic layers had a (2 × 2) lateral periodicity with (111) exposed surface, and the slab replica was separated by ∼20 Å of vacuum. The Bi-doped Cu slab models were built by replacing a surface Cu atom with Bi metal atoms. A uniform 2 × 2 × 2 k-mesh grid in the Brillouin zone was used to optimize the slab structures of Cu and Bi-doped Cu without and with molecular adsorption. The kinetic energy cutoff for the wave functions was set at 450 eV. All the atomic positions of the Cu and Bi-doped Cu without and with molecular adsorption were relaxed until the forces on each atom were less than 0.01 eV/Å. The Gibbs free energy change (ΔG) was calculated by the computational hydrogen electrode (CHE) model as follows:

https://doi.org/10.1021/acscatal.5c01960
ACS Catal. 2025, 15, 8966−8978

$$\Delta G = \Delta E_{DFT} + \Delta E_{ZPE} - T\Delta S$$

where ΔE_{DFT} represents the reaction energy, determined as the total energy difference between the reactant and product molecules absorbed on the catalyst surface; ΔE_{ZPE} is the zero-point energy correction to the Gibbs free energy; ΔS is the entropy change with each reaction; and T corresponds to room temperature (298.15 K).

■ ASSOCIATED CONTENT

Supporting Information

The Supporting Information is available free of charge at https://pubs.acs.org/doi/10.1021/acscatal.5c01960.

Experimental procedures and characterization data; additional experimental details; TEM, XPS, EXAFS, and PXRD data for Cu−$Bi_{0.1}$, Cu−$In_{0.1}$, and Cu−$Pb_{0.1}$ nanoalloys; cyclic voltammograms; electrochemical stability measurements; postreaction analyses; isotope-labeling in situ ATR-FTIR spectroscopy measurements; quantification of urea, ammonia, and nitrite; and crystallographic data for Cu−$Bi_{0.1}$ (PDF)

■ AUTHOR INFORMATION

Corresponding Authors

Qiong Lei − *Macao Institute of Materials Science and Engineering (MIMSE), Faculty of Innovation Engineering, Macau University of Science and Technology, Taipa, Macao 999078, China;* orcid.org/0000-0002-7285-9901; Email: qlei@must.edu.mo

Jun Yin − *Department of Applied Physics, The Hong Kong Polytechnic University, Hong Kong 999077, China;* orcid.org/0000-0002-1749-1120; Email: jun.yin@polyu.edu.hk

Tsz Woon Benedict Lo − *State Key Laboratory of Chemical Biology and Drug Discovery, Department of Applied Biology and Chemical Technology and Department of Applied Physics, The Hong Kong Polytechnic University, Hong Kong 999077, China; PolyU-Daya Bay Technology and Innovation Research Institute, The Hong Kong Polytechnic University, Huizhou, Guangdong, China;* orcid.org/0000-0002-4853-0196; Email: benedict.tw.lo@polyu.edu.hk

Authors

Hao Zhang − *State Key Laboratory of Chemical Biology and Drug Discovery, Department of Applied Biology and Chemical Technology, The Hong Kong Polytechnic University, Hong Kong 999077, China*

Jinjie Liu − *Department of Applied Physics, The Hong Kong Polytechnic University, Hong Kong 999077, China*

Zhihang Xu − *Department of Applied Physics, The Hong Kong Polytechnic University, Hong Kong 999077, China*

Yuanzhi Bu − *State Key Laboratory of Chemical Biology and Drug Discovery, Department of Applied Biology and Chemical Technology, The Hong Kong Polytechnic University, Hong Kong 999077, China*

Tai-Sing Wu − *National Synchrotron Radiation Research Center, Hsinchu 30076, Taiwan, R. O. C.;* orcid.org/0000-0002-3285-7258

Wei-Min Tu − *Department of Physics, National Tsing Hua University, Hsinchu 30013, Taiwan, R. O. C.*

Yun-Liang Soo − *Department of Physics, National Tsing Hua University, Hsinchu 30013, Taiwan, R. O. C.*

Cong Lin − *State Key Laboratory of Chemical Biology and Drug Discovery, Department of Applied Biology and Chemical Technology, The Hong Kong Polytechnic University, Hong Kong 999077, China;* orcid.org/0000-0003-0021-5055

Ye Zhu − *Department of Applied Physics, The Hong Kong Polytechnic University, Hong Kong 999077, China*

Complete contact information is available at: https://pubs.acs.org/10.1021/acscatal.5c01960

Notes

The authors declare no competing financial interest.

■ ACKNOWLEDGMENTS

T.W.B.L. acknowledges financial support from the National Natural Science Foundation of China (22172136), the Hong Kong Research Grants Council (15305722, 15301521, and 15300819), PolyU fund (P0042930, P0039335, P0042646). We thank NSRRC (2020-2-030-1, 2020-2-030-2, and 2020-2-030-3), and SPring-8 (2018A1253, 2022B0545, 2023B1665 and 2023B1666) for beamtimes; UMF, UCEA, ULS of HKPU for the support in material characterization. J.Y. acknowledges financial support from Hong Kong Polytechnic University (P0042930, P0049027, P0050410, and P0053682), Research Grants Council of the Hong Kong Special Administrative (SAR) Region, China (Project No. PolyU 25300823 and PolyU 15300724), and National Natural Science Foundation of China (62422512). Q.L. acknowledges financial support from the Science and Technology Development Fund of the Macau SAR, China (No. 0056/2024/RIB1).

■ REFERENCES

(1) Hu, Q.; Zhou, W.; Qi, S.; Huo, Q.; Li, X.; Lv, M.; Chen, X.; Feng, C.; Yu, J.; Chai, X.; Yang, H.; He, C. Pulsed co-electrolysis of carbon dioxide and nitrate for sustainable urea synthesis. *Nat. Sustain.* **2024**, *7* (4), 442−451.

(2) Meng, N.; Ma, X.; Wang, C.; Wang, Y.; Yang, R.; Shao, J.; Huang, Y.; Xu, Y.; Zhang, B.; Yu, Y. Oxide-Derived Core-Shell Cu@Zn Nanowires for Urea Electrosynthesis from Carbon Dioxide and Nitrate in Water. *ACS Nano* **2022**, *16* (6), 9095−9104.

(3) Xia, M.; Mao, C.; Gu, A.; Tountas, A. A.; Qiu, C.; Wood, T. E.; Li, Y. F.; Ulmer, U.; Xu, Y.; Viasus, C. J.; Ye, J.; Qian, C.; Ozin, G. Solar Urea: Towards a Sustainable Fertilizer Industry. *Angew. Chem., Int. Ed.* **2022**, *61* (1), No. e202110158.

(4) Gong, Y.; Wu, J.; Kitano, M.; Wang, J.; Ye, T.-N.; Li, J.; Kobayashi, Y.; Kishida, K.; Abe, H.; Niwa, Y.; Yang, H.; Tada, T.; Hosono, H. Ternary intermetallic LaCoSi as a catalyst for N2 activation. *Nat. Catal.* **2018**, *1* (3), 178−185.

(5) Xu, M.; Wu, F.; Zhang, Y.; Yao, Y.; Zhu, G.; Li, X.; Chen, L.; Jia, G.; Wu, X.; Huang, Y.; Gao, P.; Ye, W. Kinetically matched C-N coupling toward efficient urea electrosynthesis enabled on copper single-atom alloy. *Nat. Commun.* **2023**, *14*, 6994.

(6) Liu, X.; Jiao, Y.; Zheng, Y.; Jaroniec, M.; Qiao, S. Z. Mechanism of C-N bonds formation in electrocatalytic urea production revealed by ab initio molecular dynamics simulation. *Nat. Commun.* **2022**, *13*, 5471.

(7) Chen, C.; Zhu, X.; Wen, X.; Zhou, Y.; Zhou, L.; Li, H.; Tao, L.; Li, Q.; Du, S.; Liu, T.; Yan, D.; Xie, C.; Zou, Y.; Wang, Y.; Chen, R.; Huo, J.; Li, Y.; Cheng, J.; Su, H.; Zhao, X.; Cheng, W.; Liu, Q.; Lin, H.; Luo, J.; Chen, J.; Dong, M.; Cheng, K.; Li, C.; Wang, S. Coupling N2 and CO2 in H2O to synthesize urea under ambient conditions. *Nat. Chem.* **2020**, *12* (8), 717−724.

(8) Yuan, M.; Chen, J.; Bai, Y.; Liu, Z.; Zhang, J.; Zhao, T.; Wang, Q.; Li, S.; He, H.; Zhang, G. Unveiling Electrochemical Urea Synthesis by Co-Activation of CO2 and N2 with Mott-Schottky

Heterostructure Catalysts. *Angew. Chem., Int. Ed.* **2021**, *60* (19), 10910−10918.
(9) Zhao, Y.; Ding, Y.; Li, W.; Liu, C.; Li, Y.; Zhao, Z.; Shan, Y.; Li, F.; Sun, L.; Li, F. Efficient urea electrosynthesis from carbon dioxide and nitrate via alternating Cu-W bimetallic C-N coupling sites. *Nat. Commun.* **2023**, *14*, 4491.
(10) Zhao, Q.; Lu, X.; Wang, Y.; Zhu, S.; Liu, Y.; Xiao, F.; Dou, S. X.; Lai, W. H.; Shao, M. Sustainable and High-Rate Electrosynthesis of Nitrogen Fertilizer. *Angew. Chem., Int. Ed.* **2023**, *62* (33), No. e202307123.
(11) Lv, C.; Zhong, L.; Liu, H.; Fang, Z.; Yan, C.; Chen, M.; Kong, Y.; Lee, C.; Liu, D.; Li, S.; Liu, J.; Song, L.; Chen, G.; Yan, Q.; Yu, G. Selective electrocatalytic synthesis of urea with nitrate and carbon dioxide. *Nat. Sustian.* **2021**, *4* (10), 868−876.
(12) Muhyuddin, M.; Zuccante, G.; Mustarelli, P.; Filippi, J.; Lavacchi, A.; Elbaz, L.; Chen, Y.-H.; Atanassov, P.; Santoro, C. Electrochemical urea production using carbon dioxide and nitrate: state of the art and perspectives. *Energy Environ. Sci.* **2024**, *17* (11), 3739−3752.
(13) Wu, Q.; Dai, C.; Meng, F.; Jiao, Y.; Xu, Z. J. Potential and electric double-layer effect in electrocatalytic urea synthesis. *Nat. Commun.* **2024**, *15*, 1095.
(14) Xiong, H.; Yu, P.; Chen, K.; Lu, S.; Hu, Q.; Cheng, T.; Xu, B.; Lu, Q. Urea synthesis via electrocatalytic oxidative coupling of CO with NH3 on Pt. *Nat. Catal.* **2024**, *7* (7), 785−795.
(15) Sakamoto, N.; Sekizawa, K.; Shirai, S.; Nonaka, T.; Arai, T.; Sato, S.; Morikawa, T. Dinuclear Cu(I) molecular electrocatalyst for CO2-to-C3 product conversion. *Nat. Catal.* **2024**, *7* (5), 574−584.
(16) Albertini, P. P.; Newton, M. A.; Wang, M.; Segura Lecina, O.; Green, P. B.; Stoian, D. C.; Oveisi, E.; Loiudice, A.; Buonsanti, R. Hybrid oxide coatings generate stable Cu catalysts for CO2 electroreduction. *Nat. Mater.* **2024**, *23* (5), 680−687.
(17) Lim, C. Y. J.; Yilmaz, M.; Arce-Ramos, J. M.; Handoko, A. D.; Teh, W. J.; Zheng, Y.; Khoo, Z. H. J.; Lin, M.; Isaacs, M.; Tam, T. L. D.; Bai, Y.; Ng, C. K.; Yeo, B. S.; Sankar, G.; Parkin, I. P.; Hippalgaonkar, K.; Sullivan, M. B.; Zhang, J.; Lim, Y. F. Surface charge as activity descriptors for electrochemical CO2 reduction to multi-carbon products on organic-functionalised Cu. *Nat. Commun.* **2023**, *14*, 335.
(18) Luo, Y.; Xie, K.; Ou, P.; Lavallais, C.; Peng, T.; Chen, Z.; Zhang, Z.; Wang, N.; Li, X.-Y.; Grigioni, I.; Liu, B.; Sinton, D.; Dunn, J. B.; Sargent, E. H. Selective electrochemical synthesis of urea from nitrate and CO2 via relay catalysis on hybrid catalysts. *Nat. Catal.* **2023**, *6* (10), 939−948.
(19) Zou, Y.; Wang, S. An Investigation of Active Sites for electrochemical CO(2) Reduction Reactions: From In Situ Characterization to Rational Design. *Adv. Sci.* **2021**, *8* (9), No. 2003579.
(20) Ding, J.; Bin Yang, H.; Ma, X.-L.; Liu, S.; Liu, W.; Mao, Q.; Huang, Y.; Li, J.; Zhang, T.; Liu, B. A tin-based tandem electrocatalyst for CO2 reduction to ethanol with 80% selectivity. *Nat. Energy* **2023**, *8* (12), 1386−1394.
(21) Wan, L.; Zhang, X.; Cheng, J.; Chen, R.; Wu, L.; Shi, J.; Luo, J. Bimetallic Cu−Zn Catalysts for Electrochemical CO2 Reduction: Phase-Separated versus Core−Shell Distribution. *ACS Catal.* **2022**, *12* (5), 2741−2748.
(22) Yang, F.; Elnabawy, A. O.; Schimmenti, R.; Song, P.; Wang, J.; Peng, Z.; Yao, S.; Deng, R.; Song, S.; Lin, Y.; Mavrikakis, M.; Xu, W. Bismuthene for highly efficient carbon dioxide electroreduction reaction. *Nat. Commun.* **2020**, *11*, 1088.
(23) Chang, Q.; Lee, J. H.; Liu, Y.; Xie, Z.; Hwang, S.; Marinkovic, N. S.; Park, A.-H. A.; Kattel, S.; Chen, J. G. Electrochemical CO2 Reduction Reaction over Cu Nanoparticles with Tunable Activity and Selectivity Mediated by Functional Groups in Polymeric Binder. *JACS Au* **2022**, *2* (1), 214−222.
(24) Niu, W.; Chen, Z.; Guo, W.; Mao, W.; Liu, Y.; Guo, Y.; Chen, J.; Huang, R.; Kang, L.; Ma, Y.; Yan, Q.; Ye, J.; Cui, C.; Zhang, L.; Wang, P.; Xu, X.; Zhang, B. Pb-rich Cu grain boundary sites for selective CO-to-n-propanol electroconversion. *Nat. Commun.* **2023**, *14*, 4882.
(25) Chen, S.; Lin, S.; Ding, L. X.; Wang, H. Modified Diacetylmonoxime-Thiosemicarbazide Detection Protocol for Accurate Quantification of Urea. *Small Methods* **2023**, *7* (9), No. e2300003.
(26) Li, M.; Shi, Q.; Li, Z.; Xu, M.; Yu, S.; Wang, Y.; Xu, S. M.; Duan, H. Photoelectrocatalytic Synthesis of Urea from Carbon Dioxide and Nitrate over a Cu(2)O Photocathode. *Angew. Chem., Int. Ed.* **2024**, *63*, No. e202406515.
(27) Wu, W.; Yang, Y.; Wang, Y.; Lu, T.; Dong, Q.; Zhao, J.; Niu, J.; Liu, Q.; Hao, Z.; Song, S. Boosting electrosynthesis of urea from N2 and CO2 by defective Cu-Bi. *Chem. Catal.* **2022**, *2* (11), 3225−3238.
(28) Zhao, Y.; Shi, R.; Bian, X.; Zhou, C.; Zhao, Y.; Zhang, S.; Wu, F.; Waterhouse, G. I. N.; Wu, L. Z.; Tung, C. H.; Zhang, T. Ammonia Detection Methods in Photocatalytic and Electrocatalytic Experiments: How to Improve the Reliability of NH(3) Production Rates? *Adv. Sci.* **2019**, *6* (8), 1d109.
(29) Feng, Y.; Yang, H.; Zhang, Y.; Huang, X.; Li, L.; Cheng, T.; Shao, Q. Te-Doped Pd Nanocrystal for Electrochemical Urea Production by Efficiently Coupling Carbon Dioxide Reduction with Nitrite Reduction. *Nano Lett.* **2020**, *20* (11), 8282−8289.
(30) Gao, W.; Wu, Q.; Fan, X.; Lu, N.; Liu, Y.; Quan, X. Promoting Electrocatalytic Reduction of CO2 and Nitrate to Urea on N-Doped Porous Hollow Carbon Spheres. *ACS Appl. Mater. & Interfaces* **2024**, *16* (38), 50726−50735.
(31) Gao, Y.; Wang, J.; Sun, M.; Jing, Y.; Chen, L.; Liang, Z.; Yang, Y.; Zhang, C.; Yao, J.; Wang, X. Tandem Catalysts Enabling Efficient C-N Coupling toward the Electrosynthesis of Urea. *Angew. Chem., Int. Ed.* **2024**, *63* (23), No. e202402215.
(32) Jin, L.; Ji, R.; Wan, H.; He, J.; Gu, P.; Lin, H.; Xu, Q.; Lu, J. Boosting the Electrocatalytic Urea Oxidation Performance by Amorphous−Crystalline Ni-TPA@NiSe Heterostructures and Mechanism Discovery. *ACS Catal.* **2023**, *13* (1), 837−847.
(33) Luo, H.; Li, B.; Ma, J. G.; Cheng, P. Surface Modification of Nano-Cu2O for Controlling CO2 Electrochemical Reduction to Ethylene and Syngas. *Angew. Chem., Int. Ed.* **2022**, *61* (11), No. e202116736.
(34) Keuleers, R.; Desseyn, H. O.; Rousseau, B.; Van Alsenoy, C. Vibrational Analysis of Urea. *J. Phys. Chem. A* **1999**, *103* (24), 4621−4630.
(35) Lv, C.; Lee, C.; Zhong, L.; Liu, H.; Liu, J.; Yang, L.; Yan, C.; Yu, W.; Hng, H. H.; Qi, Z.; Song, L.; Li, S.; Loh, K. P.; Yan, Q.; Yu, G. A Defect Engineered Electrocatalyst that Promotes High-Efficiency Urea Synthesis under Ambient Conditions. *ACS Nano* **2022**, *16* (5), 8213−8222.
(36) Li, H.; Xu, L.; Bo, S.; Wang, Y.; Xu, H.; Chen, C.; Miao, R.; Chen, D.; Zhang, K.; Liu, Q.; Shen, J.; Shao, H.; Jia, J.; Wang, S. Ligand engineering towards electrocatalytic urea synthesis on a molecular catalyst. *Nat. Commun.* **2024**, *15*, 8858.
(37) Manivannan, M.; Rajendran, S. Investigation of inhibitive action of urea-Zn2+ system in the corrosion control of carbon steel in sea water. *Int. J. Eng. Sci. Technol.* **2011**, *3* (11), 8048−8060.
(38) Silverstein, R. M.; Bassler, G. C. Spectrometric identification of organic compounds. *J. Chem. Educ.* **1962**, *39* (11), 546.
(39) Tucureanu, V.; Matei, A.; Avram, A. M. FTIR Spectroscopy for Carbon Family Study. *Crit. Rev. Anal. Chem.* **2016**, *46* (6), 502−520.
(40) Bossa, J. B.; Theulé, P.; Duvernay, F.; Borget, F.; Chiavassa, T. Carbamic acid and carbamate formation in NH3:CO2 ices-UV irradiation versus thermal processes. *Astronomy & Astrophys.* **2008**, *492* (3), 719−724.
(41) Zhang, X.; Zhu, X.; Bo, S.; Chen, C.; Qiu, M.; Wei, X.; He, N.; Xie, C.; Chen, W.; Zheng, J.; Chen, P.; Jiang, S. P.; Li, Y.; Liu, Q.; Wang, S. Identifying and tailoring C-N coupling site for efficient urea synthesis over diatomic Fe-Ni catalyst. *Nat. Commun.* **2022**, *13*, 5337.
(42) Cheng, W.; Zhao, X.; Su, H.; Tang, F.; Che, W.; Zhang, H.; Liu, Q. Lattice-strained metal−organic-framework arrays for bifunctional oxygen electrocatalysis. *Nat. Energy* **2019**, *4* (2), 115−122.
(43) Zhan, C.; Dattila, F.; Rettenmaier, C.; Bergmann, A.; Kuhl, S.; Garcia-Muelas, R.; Lopez, N.; Cuenya, B. R. Revealing the CO Coverage-Driven C-C Coupling Mechanism for Electrochemical CO2

https://doi.org/10.1021/acscatal.5c01960
ACS Catal. 2025, 15, 8966−8978

Reduction on Cu2O Nanocubes via Operando Raman Spectroscopy. *ACS Catal.* **2021**, *11* (13), 7694−7701.
(44) Gajdo, M.; Eichler, A.; Hafner, J. CO adsorption on close-packed transition and noble metal surfaces: trends from ab initio calculations. *J. Phys.:Condens. Matter* **2004**, *16* (8), 1141−1164.
(45) Chernyshova, I. V.; Somasundaran, P.; Ponnurangam, S. On the origin of the elusive first intermediate of CO2 electroreduction. *Proc. Natl. Acad. Sci. U. S. A* **2018**, *115* (40), E9261−E9270.
(46) Sergent, N.; Epifani, M.; Pagnier, T. In situ Raman spectroscopy study of NO2 adsorption onto nanocrystalline tin(IV) oxide. *J. Raman Spectrosc.* **2006**, *37* (11), 1272−1277.
(47) Qiu, W.; Qin, S.; Li, Y.; Cao, N.; Cui, W.; Zhang, Z.; Zhuang, Z.; Wang, D.; Zhang, Y. Overcoming Electrostatic Interaction via Pulsed Electroreduction for Boosting the Electrocatalytic Urea Synthesis. *Angew. Chem., Int. Ed.* **2024**, *63* (24), No. e202402684.
(48) Zhou, M.; Zhang, Y.; Li, H.; Li, Z.; Wang, S.; Lu, X.; Yang, S. Tailoring O-Monodentate Adsorption of CO2 Initiates C−N Coupling for Efficient Urea Electrosynthesis with Ultrahigh Carbon Atom Economy. *Angew. Chem., Int. Ed.* **2025**, *64* (2), No. e202414392.
(49) Yao, S.; Jiang, S.; Wang, B.; Yin, H.; Xiang, X.; Tang, Z.; An, C.; Lu, T.; Zhang, Z. Polyoxometalate Confined Synthesis of BiVO4 Nanocluster for Urea Production with Remarkable O2/N2 Tolerance. *Angew. Chem., Int. Ed.* **2025**, *137* (6), No. e202418637.
(50) Yang, Q.; Cai, J.; Li, G.; Gao, R.; Han, Z.; Han, J.; Liu, D.; Song, L.; Shi, Z.; Wang, D.; Wang, G.; Zheng, W.; Zhou, G.; Song, Y. Chlorine bridge bond-enabled binuclear copper complex for electrocatalyzing lithium-sulfur reactions. *Nat. Commun.* **2024**, *15*, 3231.
(51) Moorcroft, M. J.; Davis, J.; Compton, R. G. Detection and determination of nitrate and nitrite: a review. *Talanta* **2001**, *54* (5), 785−803.
(52) Ravel, B.; Newville, M. ATHENA, ARTEMIS, HEPHAESTUS: data analysis for X-ray absorption spectroscopy using IFEFFIT. *J. Synchrotron Radiat.* **2005**, *12* (4), 537−541.

https://doi.org/10.1021/acscatal.5c01960
ACS Catal. 2025, 15, 8966−8978